Chemical Engineering Science 316 (2025) 122002

Contents lists available at ScienceDirect

Chemical Engineering Science

journal homepage: www.elsevier.com/locate/ces

# A CFD-based approach to study cavitation in high-pressure homogenizer valves. Part 1. Cavitation inception, extent and location

Eva Rütten [a], Andreas Håkansson [b,*]

[a] Institute of Process Engineering in Life Sciences, Food Process Engineering, Karlsruhe Institute of Technology, Karlsruhe, Germany
[b] Department of Process and Life Science Engineering, Lund University, Lund, Sweden

ARTICLE INFO

*Keywords:*
Cavitation
High-pressure homogenization
Emulsification
CFD

ABSTRACT

Hydrodynamic cavitation occurs in high-pressure homogenizer (HPH) valves, causes wear and influences emulsification. Substantial advances have previously been made studying HPH cavitation in experimental systems. However, there is a lack of understanding on how cavitation develops in industrially relevant valves. The series applies CFD to address this knowledge gap. This part combines a previously validated one-phase CFD model and a macroscopic cavitation model–previously seen to compare favourably to experimental cavitation visualization–to study inception, location and extent of cavitation, as a function of homogenizing pressure and Thoma number. Cavitation inception is predicted below a cavitation number of 0.20. Vapour accumulates in the large vortices of the outlet chamber, and the steady-state volume fraction of vapour accumulation decreases with cavitation number. Moreover, operating the HPH at a low Thoma number results in shifting the macroscopic flow. This helps explaining the observation of reduced emulsion breakup under extensive cavitation.

## 1. Introduction

High-pressure homogenizers (HPHs) are used to break emulsion drops, cells, cell-structures and macromolecules in many applications of food-, pharmaceutical-, and bioprocessing, as well as other applications of chemical engineering (Håkansson, 2019; Inguva et al., 2024; Levy et al., 2021; Osari-Arias et al., 2021; Ransmark et al., 2025). The typical (radial diffuser) HPH valve consists of a narrow constriction (referred to as the gap) formed by a forcer pressing down on a seat (see Fig. 1). In most industrial applications, HPHs are operated with two serially connected valves (or 'stages'). The first stage achieves the desired breakup and the second stage is used to set the backpressure to the first.

The main operating parameter is the homogenizing pressure, defined as the difference between inlet pressure $p_1$ and the backpressure, $p_2$ (as seen from the perspective of the primary valve),

$$\Delta p = p_1 - p_2 \tag{1}$$

HPH valves display hydrodynamic cavitation despite being operated with high inlet pressures (~10–100 MPa), due to the high velocity created at the gap inlet, leading to the creation of zones with low static pressure (Kurzhals, 1977; Loo et al., 1950; McKillop et al., 1955; Phipps, 1974).

Experimentally, cavitation in HPH valves has been identified from audio recordings showing high amplitude signals in the ultrasonic frequency range (resulting from imploding cavitation bubbles) (Håkansson et al., 2010; Håkansson, 2025; Kurzhals, 1977; Schlender et al., 2015), from cavitation wear (resulting from bubble collapse induced jet impingement on solid surfaces) (Innings et al., 2011), and from the formation of free-radicals (due to extreme local pressure and temperature sites of bubble implosion) (Floury et al., 2004; Lander et al., 2000; Shirgaonkar et al., 1998). Some investigators have also attempted to measure gap-height lift (resulting from cavitation bubbles present in the gap) (Innings, 2005), or to extract local pressure profiles using 'bleeding hole'-techniques (Loo et al., 1950). Regardless of the utilized method, these studies typically find that cavitation decreases with increasing backpressure and increases with the applied homogenizing pressure.

The abovementioned studies are indirect in the sense that they study the effects of cavitation (e.g., acoustic emissions and erosion wear) rather than the cavitation itself (i.e., bubble dynamics and implosions). Direct visualization of cavitation has, thus far, only been achieved in re-scaled and/or simplified valves. The first attempts were made on crudely scaled system with poor image quality (McKillop et al., 1955). Håkansson et al. (2010) provided an early direct visualization where cavitation was seen as blurry light-scattering regions in a full-scale but

* Corresponding author.
*E-mail address:* andreas.hakansson@ple.lth.se (A. Håkansson).

https://doi.org/10.1016/j.ces.2025.122002
Received 26 March 2025; Received in revised form 23 May 2025; Accepted 7 June 2025
Available online 7 June 2025

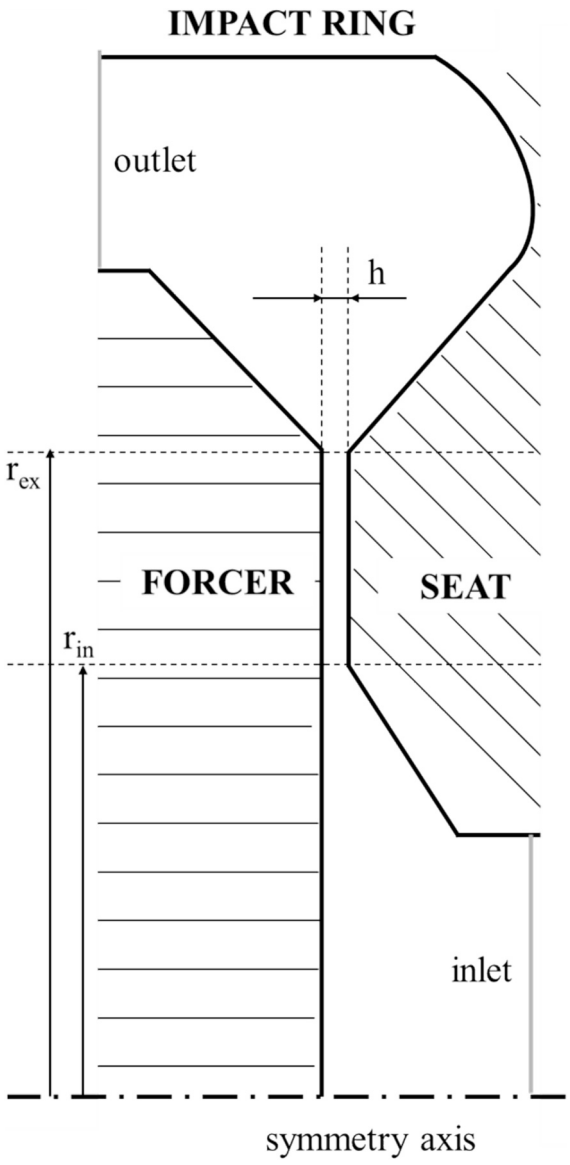


**Fig. 1.** Schematic (not to scale) sketch of an axisymmetrical HPH valve, showing the forcer, seat and impact ring as well as the definition of gap height, h, gap exit radius, $r_{ex}$, and gap inlet radius, $r_{in}$. Dash-dotted line at the bottom denotes the symmetry axis.

planar valve with optical access. More in-depth investigations using substantially higher image quality has been achieved in later studies (Gall et al., 2022; Gothsch et al., 2015, 2016; Preiss et al., 2021; Rütten et al., 2024; Schlender et al., 2015, 2016). These later studies allow for a detailed understanding of which regions of the valve that are vapour filled for different valve geometries and operating conditions.

Cavitation extent is often described in terms of a cavitation number (Brennen, 1995):

$$\sigma = \frac{p_\infty - p_v}{0.5 \cdot \rho_C \cdot U_\infty^2} \tag{2}$$

where $p_v$ is the vapour pressure, $\rho_C$ is the liquid density, $p_\infty$ is the characteristic pressure and $U_\infty$ is a characteristic velocity. For the HPH valve, we set $p_\infty = p_2$ (the backpressure) and $U_\infty = U_{in}$ (the average gap inlet velocity):

$$\sigma = \frac{p_2 - p_v}{0.5 \cdot \rho_C \cdot U_{in}^2} \tag{3}$$

In general, cavitation inception occurs when the cavitation number exceeds a critical value (Brennen, 1995; Franc and Michel, 2005). Moreover, visualization studies in modified and scaled valves show several transitions between cavitation regimes; from suppression of all cavitation at sufficiently high cavitation numbers, followed by occasional bubble formation inside the valve at intermediary cavitation numbers, and, finally, super-cavitation when the cavitation number is exceedingly low (Gothsch et al., 2015, 2016; Schlender et al., 2016). When operating at a sufficiently low cavitation number, the flow undergoes a hydrodynamic flip where most of the volume downstream of the gap is vapour filled (Schlender et al., 2016; Gothsch et al., 2015, 2016). There is, at present, no general agreement on the inception cavitation number of a HPH-valve. However, experimental estimations indicate a relatively large geometry-dependence–i.e., $\sigma = 0.5$ (Håkansson et al., 2010), $\sigma = 0.15$ (Håkansson, 2025), $\sigma = 0.53$–$0.70$ (Rütten et al., 2024) and $\sigma = 0.8$ (Gothsch et al., 2015).

While the cavitation number is a more relevant parameter from a theoretical perspective, it is not straight-forward to calculate under experimental laboratory or industrial processing conditions (since $U_{in}$ in Eq. (3) is not directly accessible in an experimental setting). Thus, the Thoma number,

$$Th = p_2/p_1 \tag{4}$$

is often used as an experimental proxy (Kessler, 2002; Kurzhals, 1977). Here it could be noted that the two quantities are related (Kessler, 2002; Kurzhals, 1977), i.e., if $p_2 \gg p_v$, if assuming all pressure losses occur at the gap exit, and if $U_{in} \approx U_{ex}$ (see derivation in Section S.3 in the Electronical Supplement),

$$\sigma \approx \frac{Th}{1 - Th} \tag{5}$$

Moreover, if further assuming that Th is 'small' (i.e., Th $\ll$ 1),

$$\sigma \approx Th \tag{6}$$

Cavitation gives rise to erosion wear in HPH valves (Innings et al., 2011). This is a major concern in industrially operated applications (Innings, 2015).

There has been a long debate in the scientific community on to what extent cavitation can also participate in, or even control, emulsion drop breakup in HPH valves (Loo et al., 1950; McKillop et al., 1955; Phipps, 1974). More generally, it is known that hydrodynamic cavitation can be very efficient in breaking emulsion drops and cells (Gode et al., 2024; Orthaber et al., 2020; Perdih et al., 2010; Thaker and Ranade, 2022, 2023). However, in HPHs, it appears that extensive cavitation has a detrimental effect on breakup (Gothsch et al. 2015; Schlender et al., 2015). More specifically, cavitation delays turbulent emulsion drop breakup (Preiss et al., 2021). The effect of modest cavitation is somewhat less clear but also appears to be detrimental (Gothsch et al., 2015). When it comes to cell disruption, some authors have argued that cavitation aids or controls breakup (Diels and Michiels, 2006; Miller et al., 2002; Shirgaonkar et al., 1998), however, many competing breakup mechanisms have been suggested and there is of yet no clear agreement in the field.

From an applied perspective, it is important to be able to predict and control the extent of cavitation, both to reduce cavitation induced erosion wear and to understand effects of cavitation on breakup efficiency. Whereas the abovementioned experimental studies are highly interesting (and have greatly advanced the field), some important challenges remain. When it comes to industrially relevant HPH valves, there is, currently, no understanding of where cavitation develops and how; all measurements on these devices are indirect (e.g., Floury et al., 2004; Kurzhals, 1977; Shirgaonkar et al., 1998). The direct visualization studies (e.g., Gothsch et al., 2016; Håkansson et al., 2010; Schlender et al., 2016), on the other hand, are on valves that differ from the industrially operated ones in many respects (i.e., they are not annular,

and they differ in terms of key geometrical factors and dimensionless numbers). Thus, cavitation inside industrially relevant valves is still poorly understood.

Computational fluid dynamics (CFD) has a great potential as a tool to understand how HPH operation and geometrical design controls fluid flow–and in extension–how this influences HPH performance. We have previously developed best-practice recommendations for CFD of industrially relevant HPH valves for non-cavitating conditions and used these to develop pressure drop correlations (Håkansson, 2024a), discuss valve design optimization (Håkansson, 2024b), and study particle impingement (Ransmark et al., 2025). However, this has been done in the absence of cavitation (i.e., corresponding to very high backpressures or cavitation number), whereas most HPHs are operated with cavitation in industrial applications.

Looking at the wider literature, there have been substantial advances in the development and application of increasingly sophisticated macroscopic models to predict cavitation (e.g., Adama Maiga et al., 2018; Feng et al., 2020; Geng and Escaler, 2020; Kinzel et al., 2019; Wang et al., 2023; Zhang et al., 2021), see Simonsen Folden et al. (2023) for a recent review. However, relatively few CFD-studies on HPH valves have included cavitation. Pang and Ngaile (2021) and Casoli et al. (2010) are two interesting exceptions. However, these studies are not based on modelling approaches that have been experimentally validated on HPH-similar devices. Recently, we have showed how a CFD model–linked to a relatively simple macroscopic cavitation model (i.e., not resolving individual vapour bubbles)–can predict the extent of cavitation and the presence or vapour filled regions in scaled-up valves (Rütten et al., 2024). At present there are no experimental techniques available for experimentally visualizing cavitation inside of the industrially relevant axisymmetrical radial diffuser valves. However, the promising results from our previous validation study suggest that a similar modelling strategy can be used to understand cavitation in these.

This contribution is the first part of two on predicting and studying cavitation in industrially relevant HPH valves using CFD. The aim of this first contribution (Part 1) is to apply a CFD-based methodology–combining our previously developed best practice conditions for cavitation-free flows (Håkansson et al., 2012; Olad et al., 2022) with aspects of our previously published cavitation modelling approach shown to compare favourably to experiments (Rütten et al., 2024)–for predicting cavitation inception, extent and location in a HPH valve. More specifically, the following research questions are addressed:

(i) How are the extent and the location of cavitation in the valve influenced by homogenizing pressure and Thoma number?
(ii) How does cavitation influence the macroscopic valve flow and how well does standard pressure loss correlations apply under cavitating conditions?
(iii) Where on the valve walls is cavitation induced erosion wear expected to occur?
(iv) How can this be used in an applied setting to better understand cavitation in HPH valves?

The second part in this series (Håkansson et al., 2025) will turn the attention to cavitation intensity.

## 2. Materials and methods

### 2.1. CFD modelling of one phase flow

First, a one-phase axisymmetric stationary CFD was setup over a valve geometry (see Fig. 1, gap exit radius $r_{ex} = 2.3$ mm, gap inlet radius $r_{in} = 1.8$ mm, inlet angle at 30° and exit angles equal to 45°) with a given and fixed gap height, following best-practice recommendations developed from validation with experimental and DNS data (Håkansson et al., 2012; Olad et al., 2022). The approach is described in previous contributions (Håkansson, 2024a, 2024b). In brief, the one-phase CFD used a Reynolds averaged Navier Stokes (RANS) RNG k-ε turbulence model (Shih et al., 1995) in a commercial solver (FLUENT 12.0, ANSYS, Canonsburg, PA) assuming an isothermal flow. An axial symmetry boundary condition was applied on the central axis. Constant velocity (based on the prescribed flowrate, set to 250 L/h) and constant pressure boundary conditions (arbitrarily set to 0 Pa) were applied on the inlet and outlet, respectively. All remaining boundaries were modelled as no-slip stationary walls using FLUENT's enhanced wall treatment option (ANSYS, 2010). The fluid density and viscosity were set to 1011 kg/m$^3$ and 0.6 mPa s, respectively.

The flow was assumed to be incompressible, which is a reasonable approximation if the Mach number is below 0.3 (Panton, 2013). In the HPH valve, local velocities are high, but the Mach number in the current cases (based on the maximum velocity across the geometry) never reached above 0.21 (and was $< 0.15$ for all cases except the highest investigated homogenizing pressure).

Meshing was carried out in a systematic and automatized stepwise sequence with built-in mesh-convergence tests (Håkansson, 2024a). In brief, a first coarse mesh was created in ANSYS Meshing, followed by a sequence of 11 consecutive mesh refinements in FLUENT (two of which refine the whole domain, three of which refine consecutively smaller regions in the (manually selected) areas of high-velocity gradients, and six of which are wall-refinements). The final mesh consisted of, approximately, 7 million cells and 450 cells across the gap height (see Håkansson (2024a) for a mesh independence study). (See Fig. S3 in the Supplement for an illustration of the mesh.).

The one-phase flow-field was initialized from zero and calculated using second order discretization schemes. The number of iterations to convergence was selected based on experience from previous studies (Håkansson, 2024a,b; Ransmark and Håkansson, 2025), and a built-in convergence test ensured that there was less than a 1 % difference in the calculated homogenizing pressure comparing 2000 to 2200 iterations.

The one-phase CFD was run for a range of gap-heights ($h$ = 15, 20, 25, 30, 35, 40 μm). The resulting homogenizing pressure (measured as the area-weighted average comparing inlet and outlet boundaries) was in the range 9–85 MPa. This is comparable to what is used in industrial applications.

### 2.2. Cavitation modelling

For each investigated condition (gap height and Thoma number), the one-phase CFD case was read and modified to have a constant static pressure boundary condition set uniformly equal to $p_1$ at the inlet and a constant static pressure boundary condition set uniformly to $p_2$ at the outlet. The pressures $p_1$ and $p_2$ were chosen so that $p_1$-$p_2$ equals the homogenizing pressure from the one-phase analysis, and so that $p_2/p_1$ equals the desired Thoma number. This approach allowed for systematically and independently studying the effect of homogenizing pressure and Thoma number. After this adjustment of the boundary conditions, the solver (still one-phase) was run for another 2000 iterations to update the one-phase (steady-state) solution.

The next step was to turn cavitation modelling on. The cavitation model was based on the setup by Rütten et al. (2024), developed from on an experimental validation using high-speed visualization of cavitating regions in a scaled-up and simplified valve design. A multiphase mixture, volume of fluids (VOF) model was selected and set to include two phases: the liquid water (primary) and the vapour (secondary).

Cavitation was modelled using the Schnerr-Sauer (Sauer and Schnerr, 2000) model with a constant vapour pressure set to $p_{vap} = 3540$ Pa. The Schnerr-Sauer model describes cavitation as a net rate of mass transfer between the liquid and vapour phases, i.e., instead of modelling the nucleation, growth and implosion of single cavitation bubbles (or clouds thereof), each computational cell is associated with a net mass transfer rate which is either a net rate of evaporation or a net rate of condensation, depending on how the static pressure relates to the

vapour pressure (in each computational cell):

$$\dot{S} = \begin{cases} C_{evap} \cdot \frac{\rho_v \cdot \rho_C}{\rho} \cdot \phi_v \cdot (1 - \phi_v) \cdot \frac{3}{R_B} \cdot \sqrt{\frac{2}{3} \cdot \frac{p_{vap} - p}{\rho}} & if p < p_{vap} \\ -C_{cond} \cdot \frac{\rho_v \cdot \rho_C}{\rho} \cdot \phi_v \cdot (1 - \phi_v) \cdot \frac{3}{R_B} \cdot \sqrt{\frac{2}{3} \cdot \frac{p - p_{vap}}{\rho}} & if p \geq p_{vap} \end{cases} \quad (7)$$

with the bubble radius given by the expression,

$$R_B = \sqrt[3]{\frac{\phi_v}{1 - \phi_v} \cdot \frac{3}{4\pi} \cdot \frac{1}{N_0}}, \quad (8)$$

and where $\rho_C$ is liquid density, $\rho_v$ is vapour density, $\rho$ is a volume fraction weighted density, $p$ is static pressure, and $\phi_v$ is the vapour volume fraction. The proportionality constants in Eq. (7) were set to $C_{evap} = 1$ and $C_{cond} = 0.2$, and the bubble number density, $N_0$, was set to $10^{11}$. No turbulence factor was included; see Rütten et al. (2024) for a motivation of these choices based on comparisons to experimental cavitation visualization in a scaled and simplified valve.

Eq. (7) enters the Navier-Stokes equations as a source term for the transport equation of the volume of fluid of the vapour phase:

$$\rho_v \frac{\partial \phi_v}{\partial t} + \rho_v \left( u_x \cdot \frac{\partial \phi_v}{\partial x} + u_y \cdot \frac{\partial \phi_v}{\partial y} + u_z \cdot \frac{\partial \phi_v}{\partial z} \right) = \dot{S} \quad (9)$$

where ($u_x$, $u_y$, $u_z$) are the coordinates of the velocity vector.

Preliminary investigations revealed that some modification was needed compared to the modelling approach in our previous study. Rütten et al. (2024) used a NIST real gas model for describing the thermodynamics of the liquid and vapour phases. This led to convergence issues and excessive computational cost when applied to the HPH valve (where domain dimension in relation to gap height is substantially larger, and where the span of static pressures is substantially higher). In the present study, the liquid water was modelled as having a constant density (1011 kg/m$^3$) and the vapour was modelled as an ideal incompressible gas. To ensure that this does not have a detrimental effect on prediction quality, a set of simulations corresponding to the validation experiments in Rütten et al. (2024) were performed with these new settings. Results show that the simplified approach overestimates the length of the cavitating region somewhat (see Fig. S1 in the Electronical Supplement). However, the trend and general appearance is consistent.

The solver was set to use a coupled velocity–pressure algorithm. QUICK was used for the momentum, the volume fraction and the turbulent quantities. PRESTO! was used for the pressure and a least-squares cell-based solver was used for spatial discretization.

Simulations were carried out in a steady-state solver. A comparison to solutions using a transient solver (i.e., running an URANS) showed no substantial difference in terms of the conclusions on where vapour accumulates or to what extent (see Supplement S5), but led to a substantially higher computational cost.

The two-phase CFD was solved for 10,000 iterations before deemed to be sufficiently converged (corresponding to approximately 400 CPU-hours on a 32-core workstation for each combination of gap-height and Thoma number). The solver was iterated until the residuals appeared visually flat. To further ensure that the steady-state solution was converged, caparisons were made between relevant variables after 10,000 and 12,000 iterations (using the case with Th = 5 %, $\Delta p$ = 25 MPa as an example). Since the difference was relatively low (flowrate: 0.42 % and mass-weighted average of volume fraction of vapour: 7 %), the solution was deemed to be converged at 10,000 iterations.

The results of a mesh comparison study (including cavitation modelling), comparing the fine mesh (utilized in the rest of the study), and a mesh with half the number of cells per gap height (i.e., a fourth of the number of cells in total) can be seen in the Supplement (Section S.2). The comparison shows that the contour plots of vapour volume fraction are similar and that the relative error (comparing coarse to fine mesh) is relatively small (volume fraction of vapour: <6 %). Thus, the mesh resolution is deemed sufficient for the purposes of the current study.

### 2.3. Cavitation numbers and estimation from a pressure loss correlation

The typical definition of a HPH valve cavitation number (Eq. (3)) is based on using the average inlet velocity as the velocity-scale (i.e., $U_\infty = U_{in}$). Since the denominator in Eq. (3) represents the maximum increase in kinetic energy, it makes sense to define a velocity corrected cavitation number where the highest local velocity magnitude $U_{max}$ is used as the velocity-scale instead:

$$\sigma^* = \frac{p_2 - p_v}{0.5 \cdot \rho_C \cdot U_{max}^2} \quad (10)$$

In the CFD-setting, $U_{max}$ is readily available, and the CFD-results will primarily be discussed in terms of this velocity corrected cavitation number. Note that, generally, $\sigma > \sigma^*$, since $U_{max} > U_{in}$.

From an applied perspective, however, the traditional HPH valve cavitation number, $\sigma$, is more useful, since $\sigma$ can be calculated using relatively simple method (i.e., without having access to CFD), as follows: Given a valve geometry (i.e., provided $r_{ex}$ and $r_{in}$), operating conditions ($\Delta p$ and flowrate) and fluid properties (density and viscosity), the resulting gap height, and gap velocities can be (implicitly) calculated by solving for them in a pressure loss correlation-equation (Håkansson, 2024a; Phipps, 1975) (see Section S.4 in the Supplement for a full set of equations). This approach allows for calculating $U_{in}$ for any set of operating conditions. Thus, it also allows for calculating $\sigma$. This approach is used in the present study to discuss and compare the effect of operating parameters on cavitation under industrial conditions (in Section 3.8).

## 3. Results and discussion

### 3.1. Vapour volume fraction and macroscopic flow – effect of Thoma number

Fig. 2 displays the steady-state vapour volume fraction at nine different Thoma numbers (Fig. 2B), together with the velocity magnitude contours under the same conditions (Fig. 2A), while keeping homogenizing pressure constant ($\Delta p$ = 26 MPa). When the Thoma number is high (Th > 15 %), there is little, or no vapor accumulated inside the valve (Fig. 2B). Moreover, the velocity field (Fig. 2A) is similar to what has been seen in previous studies (experimental and numerical) conducted in the absence of cavitation (Håkansson, 2024a; Håkansson, 2024b; Innings and Trägårdh, 2007): fluid bends off radially (i.e., upwards in Fig. 2) and is accelerated radially into the gap. Further downstream, fluid exits the gap creating a turbulent jet that bends off towards the forcer incline (i.e., to the left in Fig. 2A).

Running the HPH at a lower Thoma number (8 % < Th < 15 %), results in that some vapour is accumulated in the recirculation vortex between the bending jet and the forcer wall. However, the macroscopic flow-field remains (qualitatively) similar. If running the HPH at a lower Thoma number still (6 % < Th < 8 %), more vapour is accumulated in the forcer wall vortex. Moreover, an increasing amount of vapour accumulates inside the large recirculation vortex formed between the jet and the chamber walls. This has a pronounced effect on the macroscopic flow. The inner vortex pushes the jet out from the forcer wall. At Th = 6 %, the jet no longer attaches to the forcer incline.

Operating the HPH at a lower Thoma number still (Th < 6 %), leads to the accumulation of more vapour in the outlet chamber. At Th = 3 %, the extensive vapour filled regions have completely lifted the jet from the forcer, turning it into a free jet. At Th = 1 %, vapour fills much of the outlet chamber resulting in what Gothsch et al. (2015, 2016) refers to as a one-pocket choked cavitating flow in the outlet chamber. However, note that the gap remains virtually free of accumulated vapour even at

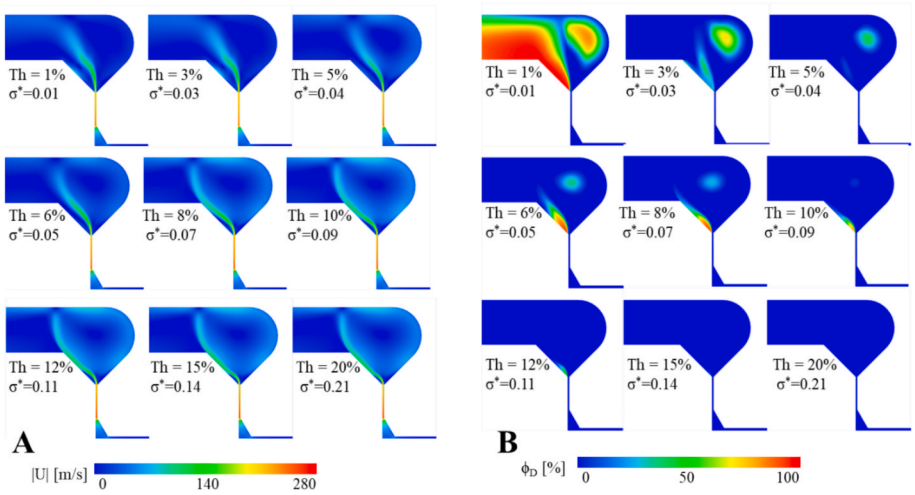


**Fig. 2.** (A) Velocity magnitude contours and (B) volume fraction of vapour contours, at varying Thoma numbers (Th = 1–20 %) while keeping the homogenizing pressure constant (Δp = 26 MPa). Corrected cavitation number, σ*, displayed for each case.

the lowest investigated back-pressure ratio (see Fig. 3), as discussed in Section 3.5.

A more quantitative investigation of the effect of Thoma number on the amount of vapour trapped inside the valve can be seen in Fig. 4A, displaying the volume integral of the vapour volume fraction. As seen in Fig. 4A, the vapour content decreases exponentially with increasing Thoma number. This finding is not surprising; it is in line with empirical evidence of cavitation being supressed when applying a high back-pressure (Gothsch et al., 2015, 2016; Håkansson et al., 2010; Preiss et al., 2021; Rütten et al., 2024; Schlender et al., 2015, 2016). The effect is explained from that higher backpressure shifts the static pressure profile upwards, while keeping the velocities constant, thus, reducing the extent of cavitation (Jahnke, 1998; Kurzhals, 1977; Phipps, 1985).

A closer investigation of Fig. 4A also reveals a slight increase in the accumulation of vapour between Th = 5 % and 6 %. This also appears to be linked to the shift in the macroscopic flow-field which occurs close to this Thoma number (see Fig. 2B).

### 3.2. *Vapour volume fraction and macroscopic flow – Effect of homogenizing pressure*

Fig. 5 displays the effect of varying homogenizing pressure ($\Delta p$ = 9–85 MPa) while keeping the Thoma number constant at a relatively low but cavitating value (Th = 5 %). Fig. 5A shows contours of velocity magnitudes and Fig. 5B shows volume fraction of vapor. (Each velocity magnitude contour has been normalized to the corresponding gap exit velocity, $U_{ex}$, to allow for a comparison of flow outline, disregarding the overall velocity increase expected when operating at higher homogenizing pressures.).

First note that the macroscopic flow changes with homogenizing pressure in the presence of cavitation–as seen in Fig. 5A, jet detachment is promoted at lower homogenizing pressures. This contrasts with cavitation-free conditions, where the velocity field remains self-similar and typically scales with the gap exit velocity (Håkansson, 2024a). Similarly to as what was seen above when varying Thoma number, the effect is linked to a shift in the position of where the vapour is accumulated, from the forcer wall vortex at high homogenizing pressures, to the large recirculation vortex at lower homogenizing pressures (Fig. 5B).

Another noticeable feature in Fig. 5B is that there is a markedly higher accumulation of vapour (i.e., a sizeable red region) close to the forcer wall at $\Delta p$ = 42 MPa compared to both the lower and the higher homogenizing pressure. When comparing with the velocity-fields (see Fig. 5A), it appears that this effect occurs at the condition where the macroscopic jet shifts from detached to just barely wall-adherent. This is likely an effect of the formation of the relatively large but still closed off recirculation vortex that forms under conditions where the jet is just barely reattaching to the forcer wall. This both results in lower static pressure in the vortex (driving more local evaporation) and ensures that vapour cannot easily escape from the vortex into the outlet pipe (see Section S.6 in the Supplement for a more comprehensive discussion and illustrations).

Seen together, Figs. 2 and 5 show that the macroscopic behaviour of the turbulent outlet chamber jet depends on the extent of cavitation in the valve. This is an interesting observation in the light of previous investigations suggesting turbulent drop breakup taking place in this region (Innings and Trägårdh, 2005; Innings et al., 2011; Kelemen et al., 2015; Mutsch et al., 2021; Olad et al., 2023). More specifically, the presence of extensive cavitation appears to have a similar effect as having large forcer and seat outlet chamber angles, i.e., it promotes a free jet (as opposed to a bending-to-attaching jet) (Håkansson, 2024b). Since both extensive cavitation and such a valve design decrease drop breakup efficiency (Gothsch et al., 2015; Håkansson, 2024b; Preiss et al., 2021), they are possibly related to the same mechanism, i.e., a widening of the region in which turbulent kinetic energy is dissipated (Håkansson, 2024b).

Fig. 4B displays the effect of homogenizing pressure on the volume integral of vapour volume fraction in the valve. Three different Thoma numbers (Th = 1 %, 5 % and 20 %) are displayed. As seen in the figure, the volume fraction of vapour shows a relatively weak dependence on homogenizing pressure. In the logarithmic scale of Fig. 4B, there appears to be a relatively marked effect of homogenizing pressure at Th = 20 %, however, in absolute terms, the vapour volume fraction is exceedingly low regardless of pressure when operating at such a high Thoma number (see Fig. 2A for an example at $\Delta p$ = 26 MPa).

### 3.3. *Vapour volume fraction and macroscopic flow – Cavitation number*

To understand the underlying cause of the observed effect of operating conditions on the vapour volume fraction and macroscopic flow, Fig. 4C plots the CFD-predicted volume integral of vapour volume fraction for all the simulated cases as a function of the velocity corrected cavitation number, $\sigma^*$. Note that this makes all the datapoints fall, approximately, on a single line. This suggests that both operating conditions influence cavitation via their effect on the cavitation number. This complies with the general finding that cavitation number is a useful indicator for describing the extent of hydrodynamic cavitation (Brennen, 1995).

From an applied perspective, it is useful to define a criterion for when

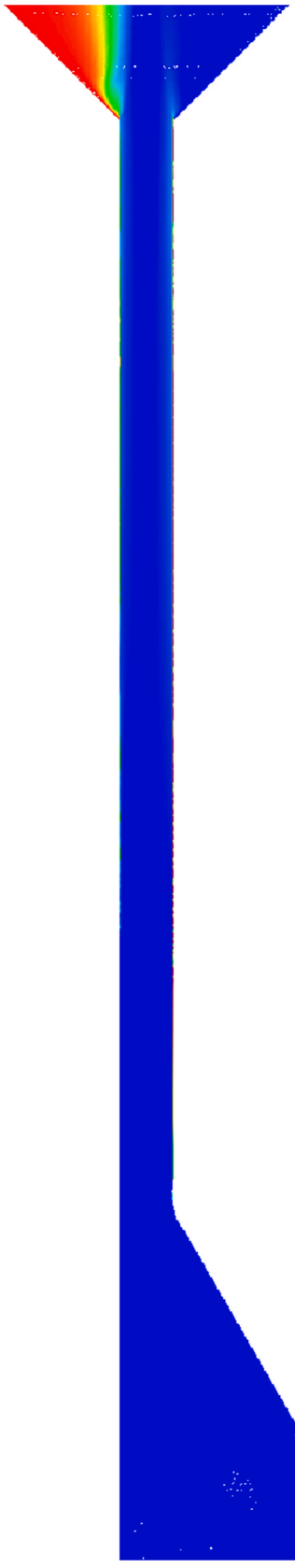

**Fig. 3.** Vapour volume fraction inside the gap at intensively cavitating conditions (Th = 1 %, Δp = 26 MPa). (Zoomed in view of the contour in Fig. 2B).

there is either no cavitation taking place in the HPH valve, or when the valve is displaying so little cavitation that it has no technical relevance. Franc and Michel (2005) define the cavitation inception number of a system as the cavitation number where cavitation can be observed in some point of the geometry. Brennen (1995), similarly, defines inception as when vapour bubble nucleation starts to occur at some position. The macroscopic CFD model does not allow for observing nucleation events or single bubble dynamics. However, Fig. 4C shows that the volume fraction of vapour decreases exponentially with cavitation number. Moreover, at $\sigma^* > 0.14$, the volume fraction of vapour is small and appears to decrease steeper with increasing Th. Thus, we define $\sigma^* = 0.14$ as the apparent inception point of the HPH valve. This is also a reasonable choice when comparing to Fig. 2B; beyond this value there is little vapour accumulation in the valve.

The link between operating conditions, cavitation number and cavitation extent can be understood more clearly by studying how the cavitation number, $\sigma$, depends on Thoma number and homogenizing pressure. Such an illustration is provided in Fig. 6 (based on gap velocity calculated from a pressure loss correlation, see Section 2.3). Fig. 6A (solid line) displays how cavitation number increases rapidly with Thoma number (under conditions of a constant homogenizing pressure). The increase is almost linear, as expected based on Eqs. (5)–(6) (these approximations have been inserted in Fig. 6 for comparison).

Homogenizing pressure has a less pronounced effect on the cavitation number. However, increasing the homogenizing pressure increases the cavitation number (if keeping Thoma number constant), as seen in Fig. 6B. The effect arises due to that the backpressure, $p_2$, is linearly dependent on the homogenizing pressure when $Th = p_2/p_1$ is kept constant (from purely algebraic reasons), whereas the inlet pressure $p_1$ increases sub-linearly with homogenizing pressure, resulting in that $\sigma$ increases with $\Delta p$. Thus, the finding in Fig. 5B, of a less pronounced cavitation (in terms or accumulated volume fraction of vapour) at higher homogenizing pressures, is consistent and expected based on the definition of the cavitation number.

Here it should also be noted that this trend of an increasing cavitation number with increasing homogenizing pressure, appears to conflict with experimental findings, which typically observe an increasing cavitation intensity when increasing homogenizing pressure (Floury et al., 2004; Håkansson et al., 2010; Kurzhals, 1977; Lander et al., 2000). This is discussed in greater detail below (see Section 3.7).

### 3.4. Applicability of standard pressure loss correlations

As mentioned above, primary hydrodynamic parameters such as gap height and gap velocities are inaccessible under industrial operation. Pressure loss correlations (Håkansson, 2024a; Jahnke, 1998; Phipps, 1975) are used to calculate these quantities from the set homogenizing pressure, flowrate and valve geometry (see Section 2.3 and Section S.4 in the Supplement). However, the correlations have been developed for conditions without cavitation, whereas cavitation is (to some extent) present in industrial scale HPHs. Thus, it is interesting to investigate under what conditions these pressure loss correlations remain good approximations in the presence of cavitation.

In the setting of the present CFD-setup, the homogenizing pressure and the gap height are set. The flowrate is allowed to adjust itself to these settings. Thus, if cavitation leads to a deviation from the pressure loss correlation, this should be observable from that the CFD-calculated flowrate, $Q$, deviates from the correlation-predicted flowrate, $Q_{pred}$.

Fig. 7A-B display $Q/Q_{pred}$ as a function of Thoma number and homogenizing pressure, respectively. ($Q$ is obtained from the cavitating CFD, $Q_{pred}$ from solving for flowrate in the pressure loss correlation, based on the known geometry and set homogenizing pressure.).

As seen from Fig. 7A, at a high Thoma number (Th > 15 %), the CFD-calculated flowrate complies, approximately, with the pressure loss correlation prediction (i.e., $Q/Q_{pred} \sim 1$). When operating at Thoma numbers below that, however, the actual flowrate is substantially lower

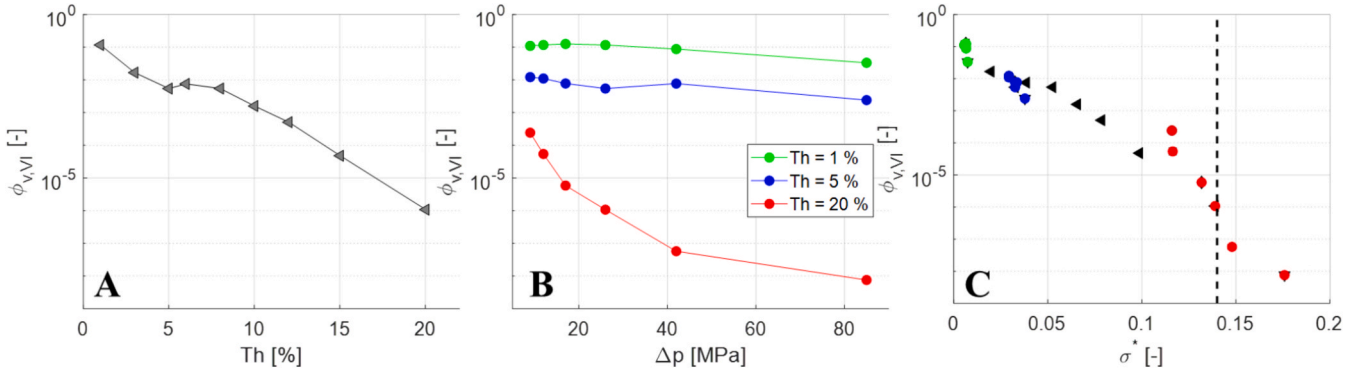


**Fig. 4.** Volume integral of vapour volume fraction in the valve, $\phi_{v,VI}$, as a function of: (A) Thoma number, Th (at Δp = 26 MPa), (B) homogenizing pressure, Δp (at Th = 1 %, 5 % and 20 %). (C) Displays the same data but plotted with corrected cavitation number, σ*, on the horizontal axis. The vertical dashed line in (C) illustrates an apparent inception point based on volume fraction of accumulated vapour in the valve (σ* = 0.14).

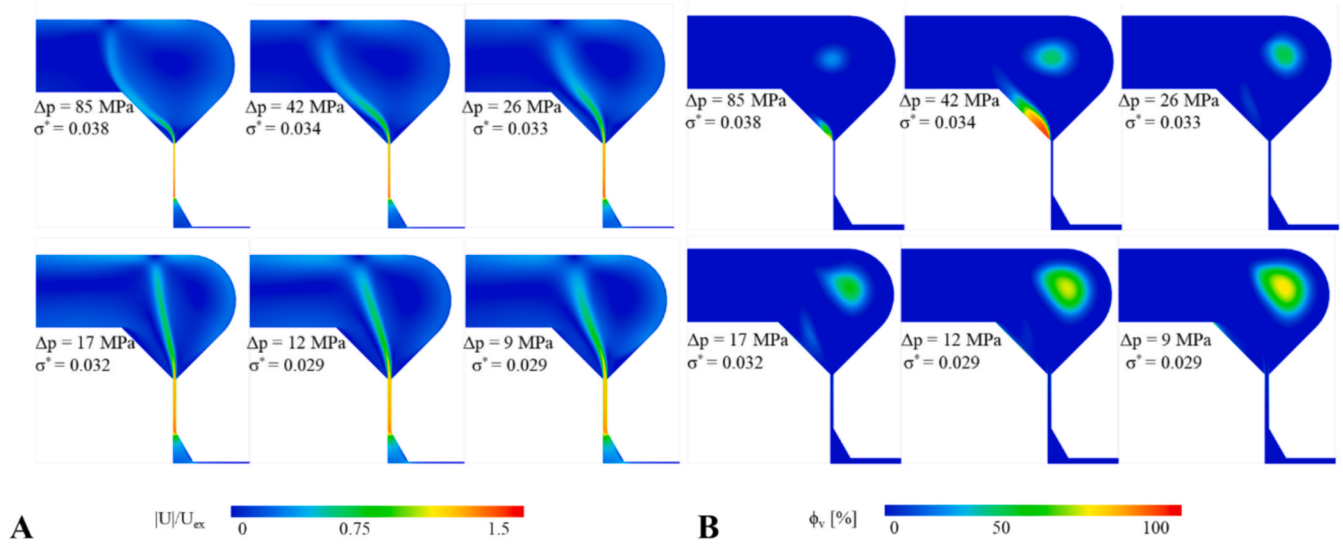


**Fig. 5.** A) Velocity magnitude contours and (B) volume fraction of vapour, at varying homogenizing pressure (Δp = 9–85 MPa) while keeping the Thoma number constant, Th = 5 %. Corrected cavitation number, σ*, displayed for each case.

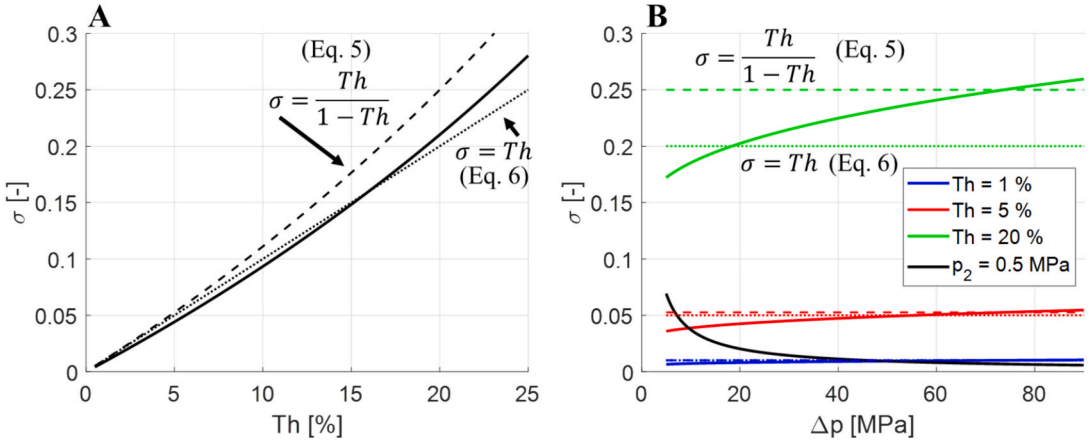


**Fig. 6.** Cavitation number, σ, as a function of Thoma number (A) and homogenizing pressure, Δp (B), with inlet velocity, $U_{in}$, calculated from a pressure loss correlation and Q = 250 L/h, $r_{ex}$ = 2.3 mm, $\rho_C$ = 1010 kg/m$^3$, $\mu_C$ = 0.6 mPa s.

than what is predicted by the correlation. This can be explained by the increased pressure losses due to the presence of vapour filled zones in the valve, which the correlations do not take into account.

Fig. 7B displays the effect of homogenizing pressure (at three levels of Th). First note that even for conditions that are effectively cavitation-free (Th = 20 %), there is small systematic error that depends on homogenizing pressure. This is not unexpected based on that the pressure loss correlation is an empirical model with an inherent uncertainty

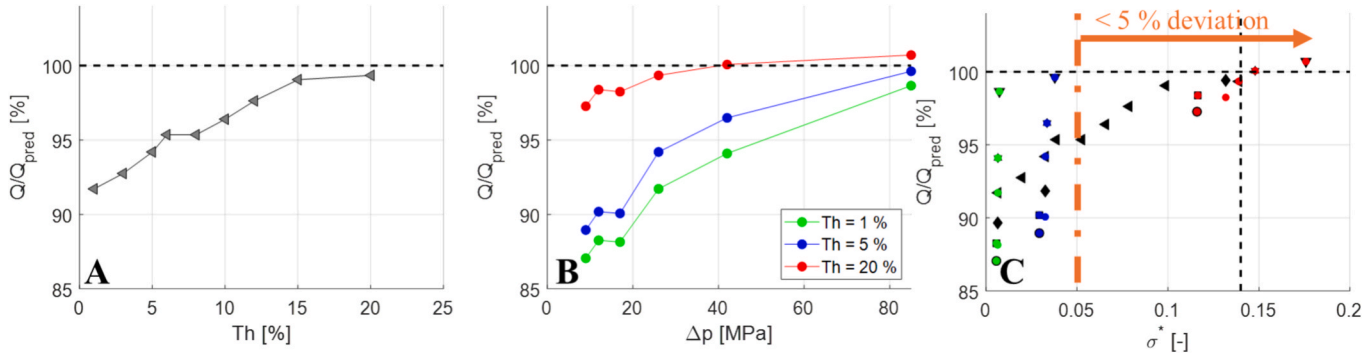


**Fig. 7.** Deviation between cavitating CFD results and pressure loss correlations, showing the CFD-calculated flowrate, Q, compared to the correlation-predicted flowrate, $Q_{pred}$, as a function of Thoma number (A) (at $\Delta p = 26$ MPa) and homogenizing pressure (B) (at Th = 1 %, 5 % and 20 %). (C) Displays the same data plotted with the corrected cavitation number, σ*, on the horizontal axis. The vertical dashed line in (C) illustrates an apparent inception point based on volume fraction of accumulated vapour in the valve (σ* = 0.14).

associated to it, see discussion in Håkansson (2024a). However, Fig. 7B shows that the deviation is amplified in the presence of cavitation.

Fig. 7C displays the same data with cavitation number on the horizontal axis. As seen in the figure, the deviation from the pressure loss correlation cannot be entirely captured by the corrected cavitation number (as could vapour volume fraction in Fig. 4C). However, it could be noted that the deviation is less than 5 % considering all cases with $\sigma^* > 0.05$ and less than 15 % for all studied cases. Thus, from a practical perspective, the pressure loss correlations developed for cavitation free conditions (Håkansson, 2024a) can be used to estimate the primary flow variables in homogenization experiments at least if $\sigma^* > 0.05$. To set this limit into a more applied context, this corresponds to operating the HPH at a Thoma number above ~6 % at 26 MPa (see Fig. 2). This is well below the 10–15 % typically used in industrial applications.

### 3.5. Position of vapour nucleation and bubble collapse

Both from a fundamental perspective, and from a design and operation optimization perspective, it is interesting to study where in the valve vapour bubbles nucleate and where they collapse. In the setting of the CFD model, the vapour nucleation can be illustrated by regions with substantial net evaporation ($\dot{S} > 1$ kg m$^{-3}$ s$^{-1}$). Similarly, regions of bubble collapse are represented by condensing regions ($\dot{S} < -1$ kg m$^{-3}$ s$^{-1}$).

Fig. 8B displays bubble nucleation regions in red and bubble collapse regions in blue, when varying Thoma numbers while keeping homogenizing pressure constant ($\Delta p = 26$ MPa). First note that regardless of Thoma number, vapour bubble nucleation is predicted in a zone close to the gap entrance. Also note that nucleation is predicted all the way from the seat wall to the forcer wall. Moreover, the point of highest evaporative mass-flow (i.e., where the driving force for nucleation is the highest), is found at the set wall of the gap entrance (see red symbols in Fig. 8A) and is independent of the applied Thoma number (Thoma number annotations are omitted in Fig. 8A since all markers are on top of each other). This is expected because of the separation zone close to the seat wall (Jahnke, 1998; Håkanson, 2022; Phipps, 1974), leading to high local velocities and a region of low pressure inside of the separation zone recirculation vortex. Moreover, this complies with suggestions in many previous studies on where cavitation nucleation in HPH valves is expected (e.g., Loo et al., 1950; McKillop et al., 1955; Phipps, 1974; Rütten et al., 2024).

Fig. 8B also shows that the lower is the backpressure, the further does this apparent nucleating region extend throughout the gap, until at Th < 8 % vapour bubble nucleation is seen throughout the gap.

Here it is interesting to note the apparent contrast with attempts to understand where cavitation takes place by only considering volume fraction. As seen in Fig. 3, vapour does not accumulate in the gap, even at the lowest investigated Thoma number. This, however, does not signify that cavitation does not take place here (as apparent from the high evaporative flux, especially at the seat entrance). The low steady-state volume fraction of vapour (Fig. 3) is a consequence of that the velocities at these positions are exceedingly high. Thus, despite vapour being generated here (at high rates), the vapour is rapidly transported into the outlet chamber, where it accumulates in recirculation vortices. This behaviour also has some methodological implications, in helping to

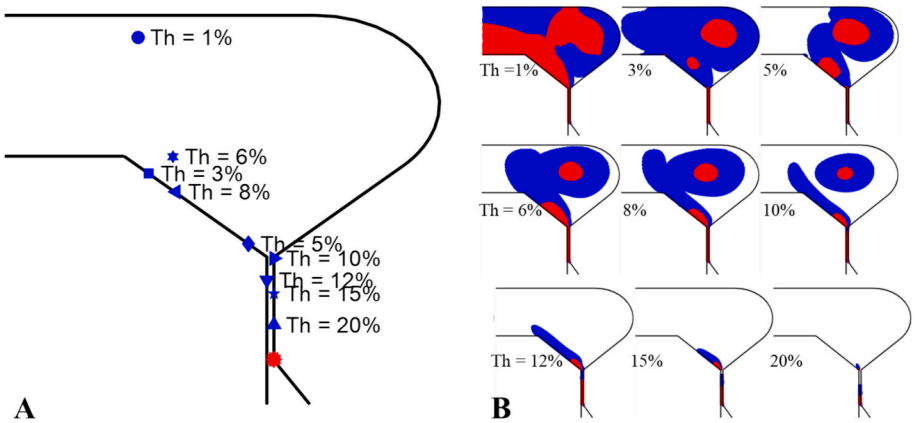


**Fig. 8.** A) Position of the highest evaporation rate (red) and condensation rate (blue) when operating the HPH valve with different Thoma numbers (1–20 %) and keeping homogenizing pressure constant (Δp = 26 MPa). B) Regions of the valve showing sizeable evaporation (red) or condensation (blue) at the nine different Thoma numbers.

explain why the steady-state solution is relatively slow to converge (see discussion in Section 2.2).

Here it could also be noted that the scale of the device matters for this effect. This can also explain why some previous studies on scaled systems show a sizable vapour volume inside the gap (Gothsch et al., 2015, 2016; Rütten et al., 2024) in contrast to Fig. 3. The mass of vapour being formed per mass of fluid entering the gap can be obtained by multiplying $\dot{S}$ with the volume of the gap and dividing by $Q{\cdot}\rho_C$. For an axisymmetrical valve, this corresponds to:

$$\frac{\dot{S}{\cdot}h{\cdot}\pi\left(r_{ex}^2 - r_{in}^2\right)}{Q{\cdot}\rho_C} \tag{11}$$

As a rough estimation, assume that the net evaporation rate at the seat wall ($\dot{S}$ in kg vapour $m^{-3}$ $s^{-1}$) is independent of scale. This is a reasonable approximation since the static pressure field is expected to be approximately independent of scale, as long as the homogenizing pressure and Thoma number are the same. Thus, the mass of vapour generated per fluid mass entering is proportional to,

$$\frac{h{\cdot}\pi\left(r_{ex}^2 - r_{in}^2\right)}{Q{\cdot}\rho_C} \tag{12}$$

This quantity is, approximately, a factor 30 larger in, for example, the scaled-up model studied by Rütten et al. (2024) than in the device investigated in the present study. Thus, although vaporization is fast, it is not fast enough (relative to the gap flowrate) to give any substantial build-up of vapour inside the gap when considering an axisymmetrical device with a high flowrate.

Returning to Fig. 8B, bubble nucleation is also seen downstream of the gap exit, inside the two recirculation vortices (see red regions). This is expected because of the low static pressure in these regions. At high to intermediary Thoma numbers, nucleation is seen inside the smaller recirculation vortex next to the forcer wall. Naturally, this nucleation zone follows the position of the vortex and, thus, detaches from the forcer wall when Th < 6 %. The last nucleation zone is inside the larger vortex, and this grows larger the lower is the Thoma number (see Fig. 8B).

Turning to the regions of vapour collapse (as indicated by regions where the net interphase transport is from vapour to liquid, indicated by blue in Fig. 8B), these are typically found just downstream of and surrounding nucleating zones. At high Thoma numbers, bubble collapse is mainly predicted inside of the gap, just downstream of the nucleation zone. Operating the HPH at a lower Thoma number result in larger bubble collapse regions in the outlet chambers.

The blue markers in Fig. 8A display the position of the highest local condensation rate for the different Thoma numbers. Note that this position shifts with the Thoma number (as opposed to the position of maximum evaporation). In the range Th = 10–20 %, the most intense collapse occurs inside of the gap. The position moves closer to the gap exit the lower is the Thoma number. Operating at a lower Thoma number moves the position of most intense bubble collapse out into the outlet chamber. In the range Th = 3–8 %, the highest condensation rates are found in the outlet chamber jet–more specifically, at the forcer wall. However, there is no consistent trend with Th within the range. This is likely linked to the behaviour seen in Fig. 2; Thoma number controls the amount of vapour that accumulates in the outlet chamber, which, in turn, shifts the position of the jet. Finally, if a very low Thoma number is applied (Th = 1 %), condensation/collapse occurs throughout the outlet chamber and the most forceful implosions are predicted close to the impact ring.

### 3.6. Prediction of regions displaying forceful microjets

Experimental investigations have observed cavitation induced erosion wear in HPH valves and suggest that this occurs due to the impact of high velocity microjets following the asymmetrical implosion of vapour bubbles close to the solid walls (Innings et al., 2011). The macroscopic net-evaporation/condensation approach used to model cavitation in the present study does not resolve individual bubbles, thus, it cannot be used to directly calculate, visualize, or quantify these microjets. However, it has previously been suggested that microjet regions can be predicted from macroscopic CFD; e.g., Peters et al. (2015) predicted microjets to emerge in regions where the volume fraction of vapour is high (i.e., vapour bubbles are present) and the static pressure is high (i.e., there is a large driving force for implosion).

Fig. 9 displays the regions (in blue) where the volume fraction of vapour is at least 1 % and static pressure is above 0.39 MPa. (These specific limits are based on suggestions provided by Peters et al. (2015); however, modifying them to $\phi_v > 5$ % and $p_{stat} > 0.1$ MPa, does not substantially alter the conclusions.).

The block arrow annotations highlight solid surfaces in direct proximity to potential microjet regions (i.e., surfaces predicted to be prone to cavitation erosion wear). Starting at conditions where a high Thoma number is applied (Th > 15 %), microjets are only predicted inside the gap.

Operating the HPH at a lower Thoma number (6 % ≤ Th ≤ 15 %), moves the microjet region to the forcer-jet. Throughout the range, microjet regions are predicted at the forcer, although the size and position on the forcer wall shows no clear and systematic dependence on the Thoma number.

At Th = 5 %, the shift of the macroscopic flow (i.e., the detachment of the jet from the forcer wall) also results in a shift of the predicted microjet positions. At Th < 3 %, the micro-jet region moves downstream, to inside the outlet chamber, even reaching the impact ring. Thus, under such conditions, cavitation erosion wear is expected to occur on the impact ring.

Unfortunately, there have only been a few empirical investigations of erosion wear in HPHs. However, Innings et al. (2011) compared wear in the absence of added particles (i.e., mainly due to cavitation) at three Thoma numbers (Th = 20 %, 10 % and 0 %), designed to result in what the authors refer to as a 'low, 'medium' or 'high' cavitation extent. For 'high' and 'medium' cavitation extent, the empirical data fits well with the predictions in Fig. 9; the experiments show cavitation erosion mainly

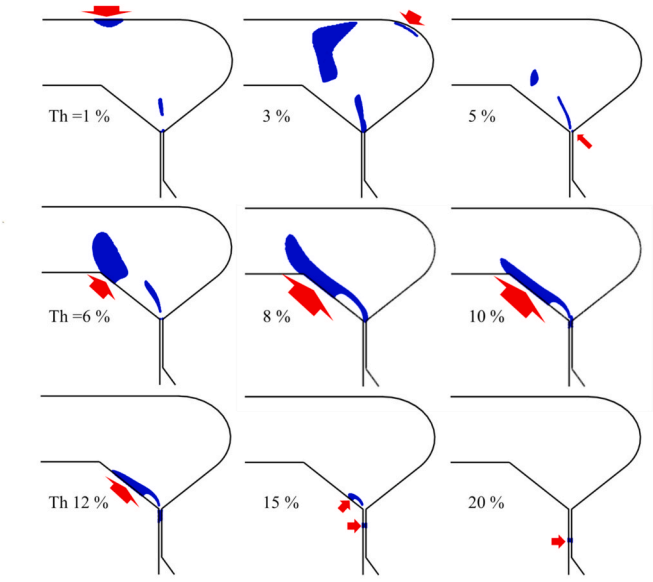


**Fig. 9.** Regions predicted to display sizeable microjets (based on the method suggested by Peters et al. (2015) using $\phi_v = 1$ % and $p_{stat} = 0.39$ MPa, as critical values) when operating at various Thoma number (at $\Delta p = 26$ MPa). Block arrows are (manually inserted) indication of where micro-jet occur sufficiently close to solid surfaces to give rise to wear.

taking place at the impact ring when no backpressure is applied and in a region just downstream of the gap exit at 'medium cavitation' (although at the seat rather than at the forcer wall, probably due to that the jet can switch sides, for examples, if the valve angles are not completely symmetrical). For the 'low' cavitation conditions, the empirical data show cavitation wear in a region between that seen in 'medium' and 'high', whereas the CFD model predicts no microjets except in a small region inside the gap. However, experimental quantification of cavitation erosion at conditions with very little cavitation is challenging, and there is a risk that small quantities of particle erosion wear will dominate over cavitation erosion wear (the authors mention the risk of limestone buildup in their system). Moreover, it is difficult to understand why cavitation wear should occur at such a high Thoma number, provided the large agreement in other experimental studies of cavitation suppression at high backpressures (Gothsch et al., 2015, 2016; Håkansson et al., 2010; Preiss et al., 2021; Rütten et al., 2024; Schlender et al., 2015). Thus, the CFD-predictions of microjet regions in Fig. 9 are in relatively good agreement with experimental results of cavitation wear in HPH valves.

### 3.7. Cavitation extent and homogenizing pressure

As briefly mentioned above (Section 3.2), there is an (at least apparent) contradiction between the results presented above and experimental studies on the effect of homogenizing pressure on cavitation. Experimental studies often find that both acoustic emissions (Håkansson et al., 2010; Håkansson, 2025; Kurzhals, 1977; Schlender et al., 2015) and free-radical formation (Floury et al., 2004; Lander et al., 2000; Shirgaonkar et al., 1998) increases with homogenizing pressure, thus, indicating an increase in cavitation intensity with homogenizing pressure. However, as discussed in Section 3.2, increasing the homogenizing pressure (at constant Thoma number) increases the cavitation number, and is thus, expected to decrease the extent of cavitation.

Part of this (apparent) contradiction is due to that some experimental studies are conducted by varying homogenizing pressure while keeping the absolute value of the backpressure constant (rather than keeping the Thoma number constant). Under such conditions, the cavitation number does decrease with increasing homogenizing pressure (see solid black line in Fig. 6B, showing conditions keeping $p_2 = 0.5$ MPa). This is also seen directly from the definition of $\sigma$ (Eq. (3)); if $p_2$ is kept constant, increasing homogenizing pressure has the sole effect of increasing gap velocity ($U_{in}$) which reduces $\sigma$. A further complication when interpreting experimental data is that a clear distinction is not always made between inlet pressure, $p_1$, and homogenizing pressure, $\Delta p$, making it difficult to fully understand which studies keep Thoma number constant and which keep the (absolute value of) the backpressure constant.

Another factor explaining this (apparent) contradiction is that cavitation 'intensity' (as measured by, for example, free-radical formation and ultrasonic emissions) is not necessarily the same as cavitation 'extent' measured by valve lift, deviation from pressure loss correlations or accumulated vapour volume fraction in the valve. Cavitation intensity is discussed in more detail in the second part of this series (Håkansson et al., 2025).

### 3.8. Predicting cavitation from operating conditions

From a practical HPH design or operation perspective, it is desirable to predict the extent of cavitation from operating conditions and valve design. The results of the present study provide some insights on this. Figs. 4 and 7 shows that some (although not all, see Fig. 10C) features of the HPH valve cavitation are functions of the velocity corrected cavitation number, $\sigma^*$. Unfortunately, $\sigma^*$ is not easily accessible in an experimental (or production) setting, since the maximum fluid velocity cannot be calculated without access to a full CFD model. Thus, there is a need for translating between $\sigma$ and $\sigma^*$.

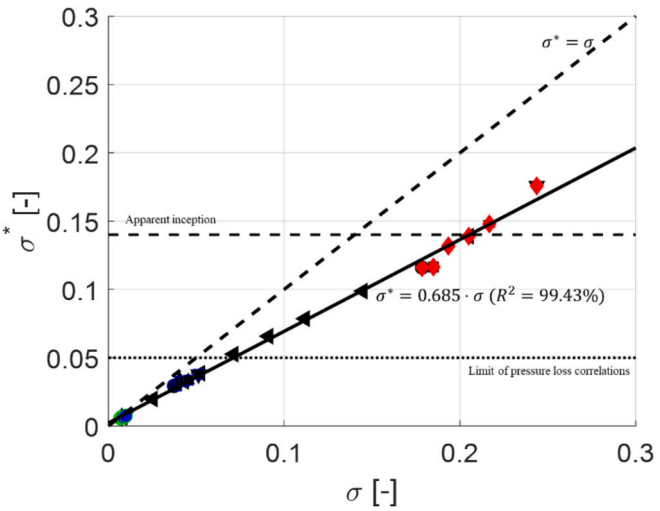


**Fig. 10.** Velocity corrected cavitation number, σ*, versus the cavitation number, σ, for the cases investigated in the present study (markers). Solid line displays a linear regression line and the dashed line displays the symmetry line (σ* = σ).

Fig. 10 displays a plot of the cavitation number, $\sigma$, and the velocity-corrected cavitation number, $\sigma^*$, for all the investigated CFD-case. As seen in Fig. 10, the velocity corrected cavitation number is linearly related to the cavitation number. From Fig. 10, an empirical relationship (by means of a least squares regression with $R^2 = 99.4$ %) is estimated to:

$$\sigma^* = 0.685 \cdot \sigma \tag{13}$$

First note that that $\sigma > \sigma^*$ as expected since $U_{in} < U_{max}$. It could also be noted that from comparing Eqs. (3) and (10), the proportionality constant in Eq. (13) equals $(U_{in}/U_{max})^2$. This empirically found value (0.685) can be compared with Jahnke (1998) suggesting 0.56 and Schlender (2015) suggesting that this ratio is in the range 0.38–0.59.

Together with the abovementioned results, Eq. (13) provides an approach for estimating cavitation extent in HPH valves based on a pressure loss correlation and some simple geometrical parameters and operating conditions. According to Fig. 7C, the pressure loss correlations are applicable at least up to $\sigma^* = 0.05$, which corresponds to $\sigma = 0.073$ (according to Eq. (13)). Comparing to Fig. 2, this limit is also, approximately, indicative of when the macroscopic jet behaviour starts to change due to the presence of cavitation.

The apparent inception point (in terms of vapour volume fraction) at $\sigma^* = 0.14$, corresponds to $\sigma = 0.20$. As mentioned above, there are large differences in the previously suggested cavitation number inception value between previous studies on HPH-valve similar devices (i.e., 0.15–0.80) (Gothsch et al., 2016; Håkansson et al., 2010; Rütten et al., 2024), possibly due to there being a strong effect of valve geometry. However, it is noteworthy that the only experimental study investigating an axisymmetrical geometry arrives at an inception point of 0.15 (Håkansson, 2025), which is similar to the CFD-based conclusion in the present study.

Fig. 11 shows how this information can be used as a first estimation to predict the effect of operating conditions on cavitation behaviour, using an industrial-scale HPH as an example ($r_{ex} = 30$ mm, $L_g = 1$ mm, $Q = 10{,}000$ L/h). Fig. 11A suggest that the valve will display a substantial extent of cavitation if (and only if) the Thoma number is less than 15–17 % in the range $\Delta p = 5$–40 MPa (the lower the homogenizing pressure, the higher is the required Thoma numbers to supress cavitation). Furthermore, to reach a cavitation extent severe enough to influence the jet orientation, backpressure ratios below 6–7 % are required.

Fig. 11B displays the effect of homogenizing pressure at four different backpressure conditions. First note that it becomes even more important to distinguish between conditions where backpressure is kept

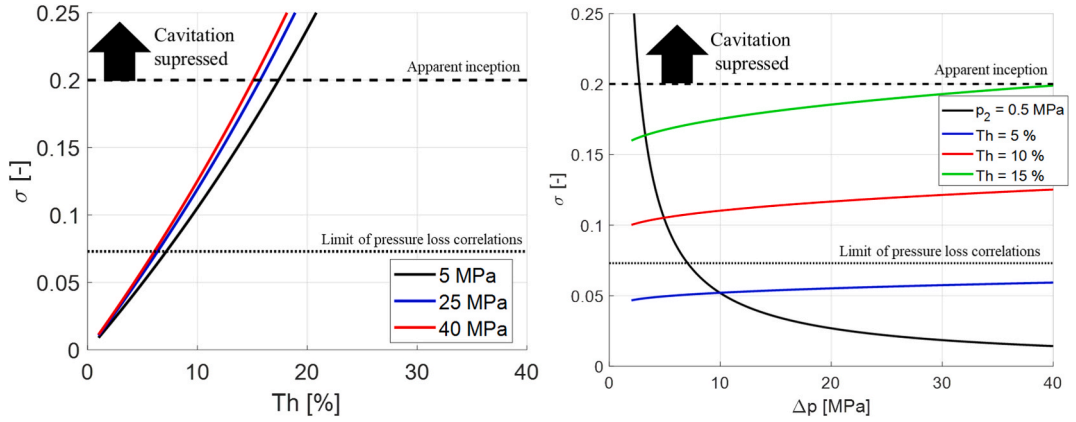


**Fig. 11.** Cavitation number, σ, as a function of Thoma number (A) (at three different homogenizing pressures) and (B) as a function of homogenizing pressure Δp (black: keeping backpressure constant at $p_2 = 0.5$ MPa, blue: keeping Th = 5 %, red: keeping Th = 10 % and green: keeping Th = 15 %) for an industrial-scale HPH valve ($r_{ex} = 30$ mm, $r_{in} = 29$ mm, Q = 10 000 L/h) (calculated based on the pressure loss correlation and Eq. (3). Dashed line shows the cavitation inception limit and dotted line shows the limit above which the pressure loss correlation deviates less than 5 %.

constant (black solid line) and conditions where Thoma number is kept constant (coloured lines) compared to the smaller device investigated in this study. When $p_2 = 0.5$ MPa, cavitation is supressed if applying a homogenizing pressure of less than 2.7 MPa. Moreover, the cavitation extent increases sharply with increasing homogenizing pressure until being extensive already at $\Delta p = 7$ MPa. Under conditions of a constant Thoma number, however, the homogenizing pressure has a limited effect on cavitation extent–increasing $\Delta p$ increases $\sigma$ slightly, thus leading to a small reduction in the homogenization extent. (However, as discussed in Section 3.7, this does not necessarily imply that cavitation intensity shows the same behaviour).

## 4. Conclusions

The aim of this contribution was to understand how operating conditions influence cavitation in industrially relevant HPH valves. The effect of both homogenizing pressure and Thoma number can be understood in terms of how they influence the cavitation number. Results indicate an apparent inception point when operating the HPH valve so that the cavitation number is below 0.20 (corresponding to Th > 15 % at $\Delta p = 26$ MPa). If operating the HPH valve at cavitation numbers below 0.07 (corresponding to Th < 7 % at $\Delta p = 26$ MPa), the macroscopic flow inside the valve is altered and the turbulent jet detaches from the forcer wall (which might help explaining the previously reported reduction in emulsion drop breakup efficiency under conditions giving rise to extensive cavitation). The standard pressure loss correlations (neglecting cavitation) can be used with fair accuracy at cavitation numbers above this. Cavitation bubble nucleation is predicted to start inside the valve regardless of operating conditions. However, the position of vapour bubble collapse and microjet creation tends to move outwards (from the gap to the impingement ring) the lower is the backpressure and cavitation number.

### Notation

| | |
|---|---|
| *Abbreviations* | |
| CFD | Computational fluid dynamics |
| DNS | Direct numerical simulation |
| HPH | High-pressure homogenization |
| HPH | Reynolds-averaged Navier-Stokes |
| *Symbols* | |
| Latin | |
| $C_{evap}$, $C_{cond}$ | Empirical constants in Eq. (7), – |
| $h$ | Gap-height, m. |
| $p$ | Static pressure, Pa. |
| $p_1$ | Inlet pressure, Pa. |

(*continued on next column*)

**Notation** (*continued*)

| | |
|---|---|
| $p_2$ | Back-pressure (to the first valve), Pa. |
| $p_\infty$ | Upstream pressure, Pa. |
| $Q$ | Flowrate, $m^3\ s^{-1}$. |
| $Q_{pred}$ | Pressure loss correlation flowrate, $m^3\ s^{-1}$. |
| $R_B$ | Bubble radius, m. |
| $r_{ex}$ | Gap exit radius, m. |
| $r_{in}$ | Gap inlet radius, m. |
| $\dot{S}$ | Evaporation/condensation flux, kg $m^{-3}\ s^{-1}$. |
| $Th$ | Thoma number (=$p_2/p_1$), –. |
| $U_{ex}$ | Gap exit velocity, m $s^{-1}$. |
| $U_{in}$ | Gap inlet velocity, m $s^{-1}$. |
| $U_{max}$ | Maximum velocity in valve, m $s^{-1}$. |
| $\|U\|$ | Velocity magnitude, m $s^{-1}$. |
| Greek | |
| $\Delta p$ | Homogenization pressure, Pa. |
| $\rho$ | Weighted-average density, kg $m^{-3}$, |
| $\rho_C$ | Liquid density, kg $m^{-3}$, |
| $\rho_V$ | Vapour density, kg $m^{-3}$, |
| $\sigma$ | Cavitation number, –. |
| $\sigma^*$ | Velocity-corrected cavitation number, –. |
| $\phi_V$ | Vapour volume fraction, – |

### CRediT authorship contribution statement

**Eva Rütten:** Writing – review & editing, Methodology, Conceptualization. **Andreas Håkansson:** Writing – original draft, Investigation, Funding acquisition, Conceptualization.

### Declaration of competing interest

The authors declare that they have no known competing financial interests or personal relationships that could have appeared to influence the work reported in this paper.

### Acknowledgment

AH acknowledges founding from the Swedish Research Counsil (VR), grant number 2024-04823.

### Appendix A. Supplementary data

Supplementary data to this article can be found online at https://doi.org/10.1016/j.ces.2025.122002.

### Data availability

Data will be made available on request.

## References


Adama Maiga, M., Coutier-Delgosha, O., Buisine, D., 2018. A new cavitation model based on bubble-bubble interactions. Phys. Fluids 30, 123301. https://doi.org/10.1063/1.5052257.

ANSYS, ANSYS FLUENT User's guide, ANSYS, Canonsburg, PA, 2010.

Brennen, C.E., 1995. Cavitation and Bubble Dynamics. Oxford University Press, Oxford.

Casoli, P., Vacca, A., Berta, G.L., 2010. A numerical procedure for predicting the performance of high pressure homogenizing valves. Simul. Model. Pract. Theory 18, 125–138. https://doi.org/10.1016/j.simpat.2009.09.014.

Diels, A.M.J., Michiels, C.W., 2006. High-pressure homogenization as a non-thermal technique for the inactivation of microorganisms. Crit. Rev. Microbiol. 32, 201–216. https://doi.org/10.1080/10408410601023516.

Feng, H., Wan, Y., Fan, Z., 2020. Numerical investigation of turbulent cavitating flow in an axial flow pump using a new transport-based model. J. Mech. Sci. Technol. 34, 745–756. https://doi.org/10.1007/s12206-020-0121-8.

Floury, J., Legrand, J., Desrumaux, A., 2004. Analysis of a new type of high pressure homogeniser. Part B. Study of droplet break-up and recoalescence phenomena. Chem. Eng. Sci. 59, 1285–1294. https://doi.org/10.1016/j.ces.2003.11.025.

Franc, J.-P., Michel, J.-M., 2005. Fundamentals of Cavitation. Springer Science, Berlin.

Gall, V., Rütten, E., Karbstein, H.P., 2022. Cavitation patterns in high-pressure homogenization nozzles with cylindrical orifices: Influence of mixing stream in Simultaneous Homogenization and Mixing. Exp. Comput. Multiphase Flow 4, 156–164. https://doi.org/10.1007/s42757-020-0088-9.

Geng, L., Escaler, X., 2020. Assessment of RANS turbulence models and Zwart cavitation model empirical coefficients for the simulation of unsteady cloud cavitation. Eng. Appl. Comput. Fluid Mech. 14, 151–167. https://doi.org/10.1080/19942060.2019.1694996.

Gode, A., Thaker, A.H., Ranade, V.V., 2024. Comparison of devices used for continuous production of emulsions: Droplet diameter, energy efficiency and capacity. Chem. Eng. Process. - Process Intesif. 203, 109881. https://doi.org/10.1016/j.cep.2024.109881.

Gothsch, T., Schilcher, C., Richter, C., Beinert, S., Dietzel, A., Büttgenbach, S., Kwade, A., 2015. High-pressure microfluidic systems (HPMS): flow and cavitation measurements in supported silicon microsystems. Microfluid. Nanofluid. 18, 121–130. https://doi.org/10.1007/s10404-014-1419-6.

Gothsch, T., Richter, C., Beinert, S., Schilcher, C., Schilde, C., Büttgenbach, S., Kwade, A., 2016. Effect of cavitation on dispersion and emulsification process in high-pressure microsystems (HPMS). Chem. Eng. Sci. 144, 239–248. https://doi.org/10.1016/j.ces.2016.01.034.

Håkansson, A., Fuchs, L., Innings, F., Revstedt, J., Bergenståhl, B., Trägårdh, C., 2010. Visual observations and acoustic measurements of cavitation in an experimental model of a high-pressure homogenizer. J. Food Eng. 100, 504–513. https://doi.org/10.1016/j.jfoodeng.2010.04.038.

Håkansson, A., Fuchs, L., Innings, F., Revstedt, J., Trägårdh, C., Bergenståhl, B., 2012. Experimental validation of k-ε RANS-CFD on a high-pressure homogenizer valve. Chem. Eng. Sci. 71, 264–273. https://doi.org/10.1016/j.ces.2011.12.039.

Håkansson, A., 2019. Emulsion formation by homogenization: current understanding and future perspectives. Annu. Rev. Food Sci. Technol. 10, 239–258. https://doi.org/10.1146/annurev-food-032818-121501.

Håkanson, A., 2022. Effect of inlet chamber design and operation conditions on laminar drop deformation in a production-scale high-pressure homogenizer—A hydrodynamic investigation. Chem. Eng. Res. Des. 180, 333–345. https://doi.org/10.1016/j.cherd.2022.02.033.

Håkansson, A., 2024a. The effect of valve design on the pressure losses in a high-pressure homogenizer – an improved pressure drop correlation for estimating gap height. Chem. Eng. Res. Des. 201, 341. https://doi.org/10.1016/j.cherd.2023.11.066.

Håkansson, A., 2024b. High-pressure homogenizer valve design modifications allowing intensified drop breakup without increasing power consumption. I. Optimization of current design-principle. Chem. Eng. Process.-Process Intensif. 196. https://doi.org/10.1016/j.cep.2023.109659.

Håkansson, A., 2025. A low-cost method for characterizing the inception and extent of cavitation in high-pressure homogenizers. Industrial & Engineering Chemistry Research Manuscript, In Press.

Håkansson, A., Rütten, E., Ranade, V.V. (2025). A CFD-based Approach to Study Cavitation in High-pressure Homogenizer Valves. Part 2. Cavitation Intensity. Second part in this series, submitted together.

Inguva, P., Grasselli, S., Heng, P.W.S., 2024. High pressure homogenization – an update on its usage and understanding. Chem. Eng. Res. Des. 202, 284–302. https://doi.org/10.1016/j.cherd.2023.12.026.

Innings, F., Trägårdh, C., 2005. Visualization of the drop deformation and break-up process in a high-pressure homogenizer. Chem. Eng. Technol. 28, 882–891. https://doi.org/10.1002/ceat.200500080.

Innings, F., Trägårdh, C., 2007. Analysis of the flow field in a high-pressure homogenizer. Exp. Therm Fluid Sci. 32 (2), 345–354. https://doi.org/10.1016/j.expthermflusci.2007.04.007.

Innings, F., Hultman, E., Forsberg, F., Prakash, B., 2011. Understanding and analysis of wear in homogenizers for processing liquid food. Wear 271, 2588–2598. https://doi.org/10.1016/j.wear.2011.01.084.

Innings, F. (2005). Drop break-up in high-pressure homogenisers. PhD-thesis. Lund University, Lund, Sweden.

Innings, F., 2015. High-pressure homogenizer design. In: Rayner, M., Dejmek, P. (Eds.), Engineering Aspects of Food Emulsification. CRC Press, Boca Raton, FL, pp. 149–168. https://doi.org/10.1201/b18436.

Jahnke, S., 1998. The theory of high-pressure homogenization. In: Benita, S., Bohm, B. (Eds.), Emulsions and Nanosuspensions for the Formulation of Poorly Soluble Drugs. CRC Press, Boca Raton, FL, USA.

Kelemen, K., Gepperth, S., Koch, R., Bauer, H.-J., Schuchmann, H.P., 2015. On the visualization of droplet deformation and breakup during high-pressure homogenization. Microfluid. Nanofluid. 19 (5), 1139–1158. https://doi.org/10.1007/s10404-015-1631-z.

Kessler, H.G., 2002. Food and Bio Process Engineering - Dairy Technology, fifth ed. Verlag A. Kessler, München.

Kinzel, M.P., Lindau, J.W., Kunz, R.F., 2019. An assessment of computational fluid dynamics cavitation models using bubble growth theory and bubble transport modeling. J. Fluids Eng. 141, 59. https://doi.org/10.1115/1.4042421.

Kurzhals, H.-A., 1977. Untersuchungen über die physikalisch-technischen Vorgänge beim Homogenisieren von Milch in Hochdruck-Homogenisiermaschinen. University of Hannover. Doctoral Thesis.

Lander, R., Manger, W., Scouloudis, M., Ku, A., Davies, C., Lee, A., 2000. Gaulin homogenization: a mechanistic Study. Biotechnol. Prog. 16 (1), 80–85. https://doi.org/10.1021/bp990135c.

Levy, R., Okun, Z., Shpigelman, A., 2021. High-pressure homogenization: Principles and applications beyond microbial inactivation. Food Eng. Rev. 13, 490–508. https://doi.org/10.1007/s12393-020-09239-8.

Loo, C.C., Slatter, W.L., Powell, R.W., 1950. A study of the cavitation effect in the homogenization of dairy products. J. Dairy Sci. 33 (10), 692–702. https://doi.org/10.3168/jds.S0022-0302(50)91958-8.

McKillop, A.A., Dunkley, W.L., Brockmeyer, R.L., Perry, R.L., 1955. The cavitation theory of homogenization. J. Dairy Sci. 38 (3), 273–283. https://doi.org/10.3168/jds.S0022-0302(55)94971-7.

Miller, J., Rogowski, M., Kelly, W., 2002. Using a CFD model to understand the fluid dynamics promoting E. coli breakage in a high-pressure homogenizer. Biotechnol. Prog. 18 (5), 1060–1067. https://doi.org/10.1021/bp020010z.

Mutsch, B., Preiss, F.J., Dagenbach, T., Karbstein, H.P., Kähler, C.J., 2021. Scaling of droplet breakup in high-pressure homogenizer orifices. Part ii: visualization of the turbulent droplet breakup. ChemEngineering 5 (2), 31. https://doi.org/10.3390/chemengineering5020031.

Olad, P., Crialesi, M., Brandt, L., Innings, F., Håkansson, A., 2022. Towards best practice recommendations for turbulence modelling of high-pressure homogenizer outlet chambers – Numerical validation using DNS data. Chem. Eng. Sci. 258, 117748. https://doi.org/10.1016/j.ces.2022.117748.

Olad, P., Innings, F., Håkansson, A., 2023. Turbulent drop breakup in a simplified high-pressure homogenizer geometry: a comparison of experimental high-speed visualization and numerical experiments based on DNS and interface tracking. Chem. Eng. Sci. 282, 119274. https://doi.org/10.1016/j.ces.2023.119274.

Orthaber, U., Zevik, J., Petkovsek, R., Dular, M., 2020. Cavitation bubble collapse in a vicinity of a liquid-liquid interface – basic research into emulsification process. Ultrasonics - Sonochemistry 68, 105224. https://doi.org/10.1016/j.ultsonch.2020.105224.

Osari-Arias, J.C., Vega-Castro, O., Martínez-Monteagudo, S.I., 2021. Fundamentals of high-pressure homogenization of foods. In: Knoerzer, K., Muthukumarappan, K. (Eds.), Innovative Food Processing Technologies. Elsevier, pp. 244–273.

Pang, H., Ngaile, G., 2021. Modeling of a valve-type low-pressure homogenizer for oil-in-water emulsions. Chem. Eng. Process. – Process Intensif. 160, 108249. https://doi.org/10.1016/j.cep.2020.108249.

Panton, R.L., 2013. Incompressible Flow. Wiley. DOI: 10.1002/9781118713075.

Perdih, T.S., Zupanc, M., Dular, M., 2010. Revision of the mechanisms behind oil-water (O/W) emulsion preparation by ultrasound and cavitation. Ultrasonics - Sonochemistry 51, 298–304. https://doi.org/10.1016/j.ultsonch.2018.10.003.

Peters, A., Sagar, H., Lantermann, U., el Moctar, O., 2015. Numerical modelling and prediction of cavitation erosion. Wear 338–339, 189–201. https://doi.org/10.1016/j.wear.2015.06.009.

Phipps, L.W., 1974. Cavitation and separated flow in a simple homogenizing valve and their influence on the break-up of fat globules in milk. J. Dairy Res. 41 (1), 1–8. https://doi.org/10.1017/S0022029900014849.

Phipps, L.W., 1975. The fragmentation of oil drops in emulsion by a high-pressure homogenizer. J. Phys. D Appl. Phys. 8, 48–462. https://doi.org/10.1088/0022-3727/8/4/018.

Phipps, L.W., 1985. The high-pressure dairy homogenizer. The National Institute for Research in Dairying, Reading, UK.

Preiss, F.J., Hetz, M., Karbstein, H.P., 2021. Does cavitation affect droplet breakup in high-pressure homogenization? Insights into local effect. Chem. Ing. Tech. 94, 374–384. https://doi.org/10.5445/IR/1000136030.

Ransmark, E., Sørensen, H., Gómez Galindo, F., Håkansson, A., 2025. Break-up of plant cell structures in high pressure homogenizers – prospects and challenges for processing of plant-based beverages. Food Eng Rev., in Press. https://doi.org/10.1007/s12393-025-09397-7.

Ransmark, E., Håkansson, A., 2025. Particle impact in high-pressure homogenizer valves – a step towards understanding wear and cell breakup in food and beverage processing. Food Bioprod. Process. 149, 1–15. https://doi.org/10.1016/j.fbp.2024.11.001.

Rütten, E., Leister, N., Karbstein, H.K., Håkansson, A., 2024. Possibilities and limits of modeling cavitation in high-pressure homogenizers – a validation study. Chem. Eng. Sci. 283, 119405. https://doi.org/10.1016/j.ces.2023.119405.

Schlender, M., 2015. Untersuchungen zum Einfluss von strömungsinduzierter Kavitation auf den Emulgierprozess bei der Hochdruckhomogenisation. Karlsruhe Institute of Technology, Karlsruhe, Germany. PhD thesis.

Schlender, M., Spengler, A., Schuchmann, H.P., 2015. High-pressure emulsion formation in cylindrical coaxial orifices: Influence of cavitation induced pattern on oil drop

size. Int. J. Multiph. Flow 74, 84–95. https://doi.org/10.1016/j.ijmultiphaseflow.2015.04.004.
Schlender, M., Minke, K., Schuchmann, H.P., 2016. Sono-chemiluminescence (SCL) in a high-pressure double stage homogenization processes. Chem. Eng. Sci. 142, 1–11. https://doi.org/10.1016/j.ces.2015.11.028.
Sauer, J., Schnerr, G.H., 2000. Unsteady cavitating flow-a new cavitation model based on a modified front capturing method and bubble dynamics. In: Proceedings of 2000 ASME Fluid Engineering Summer Conference, p. 251.
Shih, T.H., Liou, W.W., Shabbir, A., Yang, Z., Zhu, J., 1995. A new k-ε eddy-viscosity model for high Reynolds number turbulent flows. Comput. Fluids 24, 227–238. https://doi.org/10.1016/0045-7930(94)00032-T.
Simonsen Folden, T., Aschmoneit, F.J., 2023. A classification and review of cavitation models with an emphasis on physical aspects of cavitation. Phys. Fluids 35, 081301. https://doi.org/10.1063/5.0157926.
Shirgaonkar, I.Z., Lothe, R.R., Pandit, A.B., 1998. Comments on the mechanism of microbial cell disruption in high-pressure and high-speed devices. Biotechnol. Prog. 14 (4), 657–660. https://doi.org/10.1021/bp980052g.
Thaker, A.H., Ranade, V.V., 2022. Towards harnessing hydrodynamic cavitation for producing emulsions: Breakage of an oil drop in a vortex based cavitation device. Chem. Eng. Process. - Process Intesif. 180, 108753. https://doi.org/10.1016/j.cep.2021.108753.
Thaker, A.H., Ranade, V.V., 2023. Drop breakage in a single-pass through vortex-based cavitation device: Experiments and modeling. AIChE J. 69 (1), e17512. https://doi.org/10.1002/aic.17512.
Wang, Y., Zhang, F., Chen, H., Feng, Y., Shouqi, K., 2023. Influence of cavitation on energy loss in a side channel pump at different flow rates. Phys. Fluids 35. https://doi.org/10.1063/5.0149614.
Zhang, S., Chen, H., Ma, Z., 2021. A modified filter-based model for simulation of unsteady cavitating flows around a NACA66 hydrofoil. Mod. Phys. Lett. B 35, 2150032. https://doi.org/10.1142/S0217984921500329.